Al-rich Fe0.85 Al0.15 (100), (110) and (111) surface structures

Zongbei Dai, Natalia Alyabyeva, Patrizia Borghetti, Stéphane Chenot, Pascal David, Alexey Koltsov, Gilles Renaud, Jacques Jupille, Gregory Cabailh, Rémi Lazzari

Al-rich $Fe_{0.85}Al_{0.15}$(100), (110) and (111) surface structures

Zongbei Dai[1], Natalia Alyabyeva[1], Patrizia Borghetti[1], Stéphane Chenot[1], Pascal David[1], Alexey Koltsov[b], Gilles Renaud[c], Jacques Jupille[1], Gregory Cabailh[1], Rémi Lazzari[1,*]

[a] *CNRS, Sorbonne Universités, Institut des NanoSciences de Paris, UMR 7588, 4 Place Jussieu, F-75005 Paris, France*
[b] *ArcelorMittal Maizieres Research, voie Romaine, F-57280, Maizières-lès-Metz, France*
[c] *Université Grenoble Alpes, CEA, IRIG, MEM, F-38000 Grenoble, France*

Abstract

Based on previous photoemission findings, the influence of newly observed aluminum surface segregation at the low (110), (100) and (111) index surfaces of the A_2 body-centered $Fe_{0.85}Al_{0.15}$ random alloy is explored. Scanning Tunneling Microscopy, Low-Energy Electron Diffraction and Grazing-Incidence X-Ray Diffraction are combined to explore surface structures and topographies. The formation of a surface composition close to the B_2 $Fe_{0.5}Al_{0.5}$ occurs with the appearance of (i) a long-range pseudo-hexagonal incommensurate superstructure with a periodicity of ~ 18 Å on the (110) surface, (ii) a (1×1) termination on the (100) surface and (iii) a intense vicinal faceting of the (111) surface in the form of triangular pits.

Keywords: segregation, body-centered cubic alloy, FeAl

1. Introduction

Beyond their fundamental interest as transition metal aluminides, binary FeAl alloys are often used as model systems to mimic the behavior of Al-alloyed steels [1, 2]. Al-alloyed iron and steel combine high mechanical strength with good resistance to corrosion and relatively low density [3, 4, 5, 2]. Taking advantage of these properties, the steel industry

*Corresponding author
Email address: remi.lazzari@insp.jussieu.fr (Rémi Lazzari)

develops Al-alloyed grades to lighten sheets while increasing their elasticity limit and stiffness (elasticity limit/density ratio). These so-called Advanced High-Strength Steels (AHSS), that allow weight reduction of cars, are among the means used by the automotive industry to face the global challenge of CO_2 emission decrease. However, a drawback of alloying steel with highly electropositive elements such as aluminum is the tendency of these to segregate and to form a surface oxide film, which then degrades the quality of the zinc-based anticorrosive coating during the galvanization process [6, 7, 8, 9, 10, 11, 12].

Compared to the complexity of alloyed steel, the $Fe_{1-x}Al_x$ binary alloy in the form of single crystal is an ideal platform to understand the orientation dependence of segregation. In the Fe-Al phase diagram [13, 14, 15, 16], for increasing Al content, a body-centered cubic (bcc) random alloy phase A_2 in which sites are statistically occupied by Al and Fe appears first; it is followed by ordered phases of type B_2 (CsCl structure) and $D0_3$ (Heussler alloy), and by a series of complex Fe-rich phases, as shortly reviewed in Ref. [17]. In a first step toward the understanding of the alloy behavior, a previous study focused on the orientation dependence of aluminum segregation at the surface of $Fe_{0.85}Al_{0.15}$(100), (110) and (111) crystalsfor annealing temperatures between 300 K and 1100 K [18, 17]. In that temperature range, this composition corresponds to the ferritic A_2 solid solution that is also encountered in industrial steel grades, which makes the $Fe_{0.85}Al_{0.15}$ alloy an appropriate model compound for Al-alloyed steels. The novelty was the observation of a strong aluminum segregation which starts at around 700 K before reaching a steady state within the probed scale of photoemission. Whatever the orientation, the near surface composition obtained is close to the B_2 $Fe_{0.5}Al_{0.5}$ with a typical affected depth of around 25 Å, except on the (110) surface for which those figures are slightly different ($Fe_{0.6}Al_{0.4}$; $\sim$ 35 Å) [17]. Although suspected in the diffraction study of Kottcke *et al.* [19] on FeAl(100) and in the Auger measurements of Hammer *et al.* [20] on the open FeAl(111) surface, such a composition gradient in the $Fe_{1-x}Al_x$ system was never evidenced before, probably because experiments [21, 22, 23, 19, 24, 20, 25, 14, 26, 23, 27] have focused mostly on ordered FeAl alloys with higher Al contents.

The present work aims at exploring the surface structures associated with the Al-enriched low-index orientations ($Fe_{0.85}Al_{0.15}$(100), (110) and (111)). If, according to a photoemission study [17], the average surface compositions

are close to $Fe_{0.5}Al_{0.5}$, differences in bulk truncation surface atomic density ($n_S(100) < n_S(111) < n_S(110)$) are anticipated to lead to specific surface structures. The surface reconstructions are explored by Low-Energy Electron Diffraction (LEED) and Grazing Incidence X-ray Diffraction (GIXD) while STM is used to unravel the associated modification of surface topography.

2. Experimental methods

Experiments were performed in an ultra-high vacuum (UHV) set-up previously described [28, 17], that involves two connected vessels equipped with LEED (ErLEED, SPECS), STM (RT-Omicron) and XPS (Omicron EA125 under non-monochromatic excitation). STM images were acquired in constant current mode with chemically etched W tips and processed with the WsXM and Gwyddion software [29, 30, 31]. Mounted on Ta plates, the $Fe_{0.85}Al_{0.15}$ single crystals [32] were cleaned by cycles of Ar^+ sputtering followed by electron bombardment annealing [17]. The annealing duration for each chosen temperature range (specified later) was kept fixed (15 min) while heating/cooling was performed as fast as possible (~ 250 K.min^{-1}) to quench the resulting concentration profile. Bulk contaminants were below the detection level of XPS on all surfaces. Only a transient segregation of carbon in the form of stripes was oberved on the (110) orientation [28]. Due to the high reactivity of aluminum, special care was taken to minimize contamination due to residual background, the Al 2p core level being a good indicator of the associated oxidation phenomenon [18].

Complementary GIXD were performed on the UHV z-axis diffractometer of the BM32 beamline at the European Synchrotron Radiation Facility (France) [33, 34]. The (110) surface was prepared in a similar way as in the laboratory. The X-ray energy was set at $E = 18$ keV ($\lambda = 0.6888$ Å) and the incident angle to $\alpha_i = 0.14°$, a value just below the critical angle for total external reflection ($\alpha_c = 0.173°$) [35] to maximize surface sensitivity. The X-ray beam was sagittally focused on the sample with horizontal ($H = 0.4$ mm) and vertical ($V = 0.3$ mm) widths (Full Width at Half Maximum, FWHM), corresponding to divergences of $\delta_H = 1$ mrad and $\delta_V = 0.13$ mrad, respectively. The detector was a 2D MaxiPix detector (1280 $\times$ 256 pixels of size 55 μm) put at a distance of 700 mm behind a 5 mm vertical slit. The signal

integration in the region of interest on the detector gives rise to a vertical resolution of 0.08° for in-plane scans and around 1.5° for out-of-plane scans. The measured lattice parameter ($a_B = 2.89$ Å) confirmed the bulk aluminum atomic fraction through the Vegard law [36]. In both LEED and GIXS, reciprocal space coordinates (h_S, k_S, l_S) are defined in the reciprocal surface unit cell $(\mathbf{a}^*_S, \mathbf{b}^*_S, \mathbf{c}^*_S)$ for which $\mathbf{c_S}$ is normal to the surface (see Ref. [17] and Fig. S1 of Supplementary Material).

3. Results and discussion

All three $Fe_{0.85}Al_{0.15}$ surfaces show a faint (1×1) pattern after sputtering which poorly improves up to the threshold of Al surface segregation [18, 17]. In the temperature regime where photoemission gives an Al stationnary profile [17], the (110) surface reconstructs. Conversely, the other two orientations display (1×1) apparent termination.

3.1. Superstructure at the $Fe_{0.85}Al_{0.15}$(110) surface

Right after sputtering and even after annealing at 673 K (not shown), the (110) surface has a faint (1×1) LEED pattern but, above 873 K, the aluminum segregation observed by photoemission [17] parallels the appearance of a surface reconstruction. The corresponding LEED pattern (Fig. 1a) has a pseudo-hexagonal "flower"-like shape around active (1×1) reflections.

3.1.1. Commensurate/incommensurate modulations

The integrated line cuts along the $[10]_S$ and $[01]_S$ directions through the $(\bar{1}1)_S$ reflection of the LEED pattern of Fig. 1- a are shown in Fig. 2. While commensurability is verified along the $[01]_S$ direction (the superstructure involving five substrate unit cells), peaks appear at $h_S = \pm 0.12, \pm 0.56$ along the $[10]_S$ direction that is to say at a distance of $\Delta h_S = 0.44$ from the surface Bragg peaks. Whatever the beam energy, the superstructure spots are found only around Bragg spots. Such a convolution of reciprocal space nodes by superstructure ones (that also verifies the $\{10\}_S$ and $\{01\}_S$ surface extinctions) demonstrates that the commensurate and incommensurate superstructures observed in direct space along the $[0k_S]$ and $[h_S0]$ directions, respectively, stem from modulations of atomic positions and/or from the composition of the (1×1) structure. It discards the existence of Moiré pattern due to a structured overlayer on-top of the (1×1) substrate. Combining patterns taken at low energy around the $(00)_S$ reflection and the superstructure spots

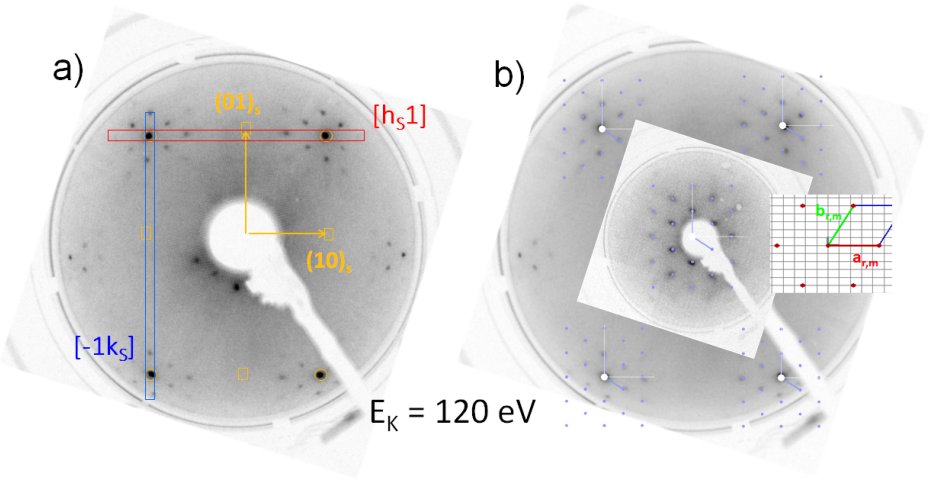

Figure 1: a) LEED pattern at $E_K = 120$ eV of a clean $Fe_{0.85}Al_{0.15}(110)$ surface annealed at 1123 K. The active and extinguished spots due to the centered rectangular surface unit cell ($h_S + k_S = 2n + 1$) are shown as circles and squares, respectively. Red and blue boxes correspond to line cuts shown in Fig. 2. b) Overlap between the LEED pattern at $E_K = 30$ eV and 120 eV with the proposed incommensurate superstructure (see text). Inset: the grey grid stands for the nodes of the (1×1) rectangular unit cell $(\mathbf{a}_S, \mathbf{b}_S)$ of direct space. The red dots are the nodes of the superstructure with basis vectors $\mathbf{a}_r$ (red) and $\mathbf{b}_r$ (green).

around $\{11\}_S$ surface reflections, the superstructure was determined with the help of the *LEEDPat* software [37]. The modulation can be described by the matrix $\begin{bmatrix} 4.55 & 0 \\ 2.27 & 5 \end{bmatrix}$ in the rectangular centered unit cell $(\mathbf{a}_S, \mathbf{b}_S)$. The "unit cell" corresponding to this modulation ($a_{r,m} = 18.6$ Å, $b_{r,m} = 17.2$ Å with an angle of $\gamma_{r,m} = 57.3°$) is a hexagon squeezed along $[01]_S$ (Fig. 1-b). Now, by convoluting all the reciprocal space substrate nodes with the LEED pattern corresponding to this matrix, the match with the LEED pattern is perfect (Fig. 1-b). Although the surface composition is close to $Fe_{0.6}Al_{0.4}$, the superstructure obtained does not match at all the small scale $FeAl_2$ reconstruction observed at the $Fe_{0.53}Al_{0.47}(110)$ surface [24, 20, 38, 39, 40].

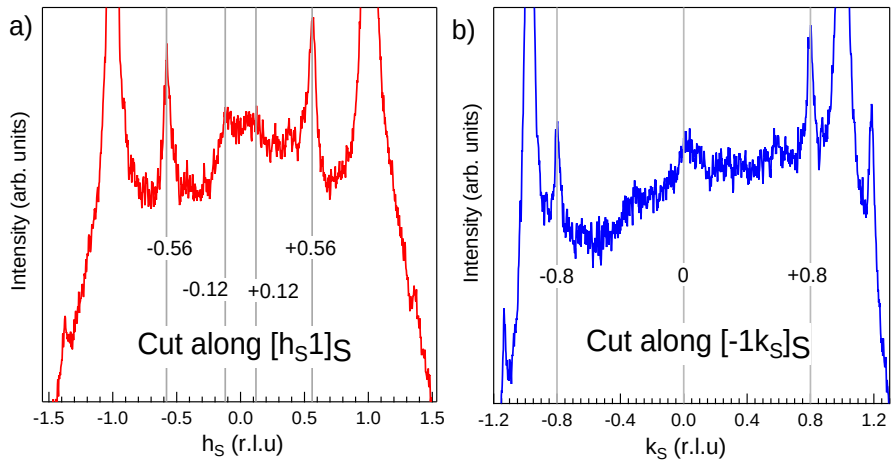

Figure 2: Line cuts of the LEED pattern of Fig. 1 along a) $[h_S 1]$ (red box) and b) $[-1 k_S]$ (blue box).

The reciprocal space directions $(h_S, 0)$ and $(0, k_S)$ were scanned by GIXS at $l_s = 0.075$ on a clean surface annealed at 1050 K (Fig. 3-a,b). The main reconstruction peaks appear at $(h_S = 1.56 - 3.56 - 5.56, 0)$ and $(0, k_S = 1.2 - 1.8 - 2.2 - 3.8 - 4.2)$ showing that the superstructure due to aluminum segregation is commensurate along the $[01]_S$ but incommensurate along the $[10]_S$. Beyond the confirmation of the LEED findings in terms of peak positions, GIXS measurements allow the estimation of the inward extension of the reconstructed layer. The out-of-plane scan at the position of the most

intense superstructure peak ($h_S = 0, k_S = 2.2$) (Fig. 3-c) has a strong modulation with an increasing broadening with l_S. An analysis of the peak FWHM Δl_S in terms of size ($\Delta l_{S,s}$) and strain ($\frac{\Delta c_r}{c_r}$) ($\Delta l_S^2 = \Delta l_{S,s}^2 + \left(\frac{\Delta c_r}{c_r}\right)^2 l^2$, inset of Fig. 3-c) leads to a variation of the lattice parameter of $\frac{\Delta c_r}{c_r} \simeq 0.2$ and a domain size of $c_S/\Delta l_{S,s} \simeq 8$ Å *i.e.* around 4 atomic layers. Such a thickness confirms that the superstructure due to the "hexagonal" modulation structure extends over several layers and does not correspond to a simple reconstructed overlayer.

3.1.2. Atomic and/or composition contrast

More has been learned on the superstructure by STM experiments. Besides the already reported transient initial segregation of carbon in the form of self-organized stripes [18, 28], annealing the (110) surface after sputtering induces a sizable smoothing, a straightening of the step edges and an increase of the average size of terraces which become mostly separated mostly by monoatomic height (2 Å) steps, suggesting that defective areas coalesce in some exent [28] (Fig. 4-a). Magnification at higher resolution clearly reveals a long-range ordered hexagonal-like superstructure [28] at 2.5 V with atomic corrugation (Fig. 4-b). The superstructure occupies the whole surface from one terrace to the other as seen in Fig. S2 of Supplementary Material and does not appear as different domains, which confirms the description with only one supercell as obtained from LEED.

It is important to mention that the chemical composition of the reconstruction and/or the presence of adsorbate on the tip strongly affect how surface is visualized by STM. Thus, a "network" like structure can only be observed at 2.5 V and above, when the current tunnels though the tip-oxide-metal heterostructure (see Fig. S3 and S4 of Supplementary Material). "Hexagons" are laterally distorted, nevertheless Fourier analysis reveals the presence of several periodicities ($\sim$ 7 Å and $\sim$ 15 Å , Fig. 4-b). Locally a hexagon-like structure can be observed (Fig. 5-a), where the 15 Å periodicity corresponds to the reconstruction unit cell (Fig. 5-a,b) in agreement with the "pseudo" hexagonal supercell found by LEED. The 7 Å distance corresponds to the drop of local conductivity (Fig. 5-a, indicated by the blue rhomb and Fig. 5-b). Atomic resolution of $Fe_{0.85}Al_{0.15}(110)$ "hexagons" evidences a complex electronic contrast that might be related to the chemical composition (Fig. 5-c). According to *ab initio* calculations [41, 42], the density of states

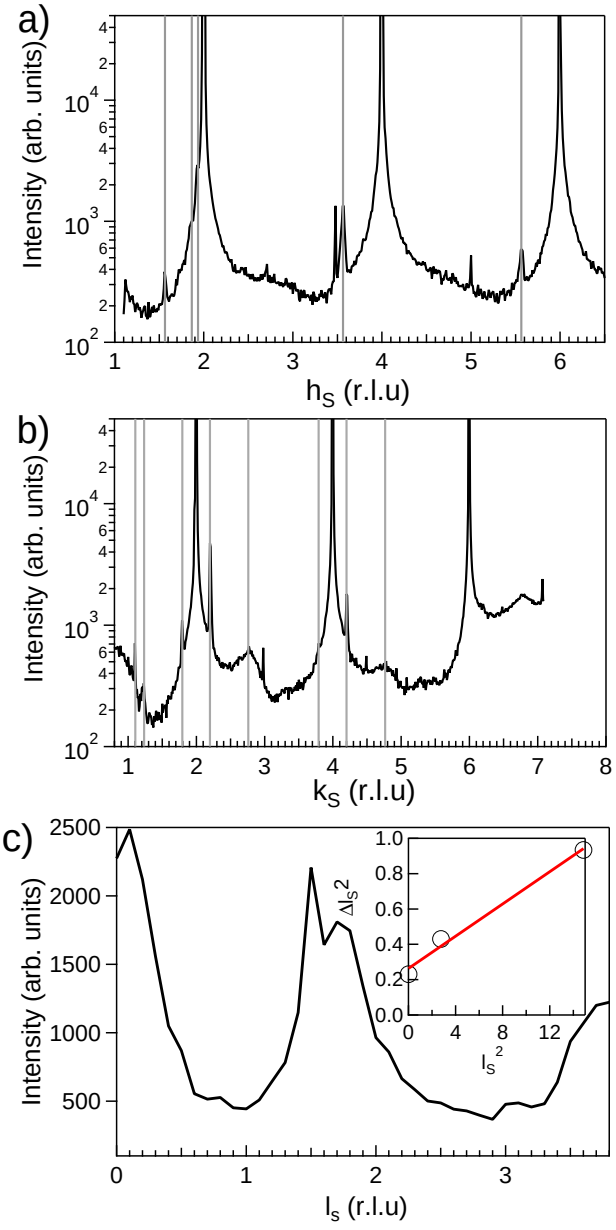

Figure 3: In plane radial diffraction scans ($l = 0.075$) of a clean $Fe_{0.85}Al_{0.15}(110)$ surface annealed at 1050 K (black line) along reciprocal directions a) $(h_S, 0, 0.075)$, b) $(0, k_S, 0.075)$. Grey lines point at peaks due to the surface reconstruction. c) Out-of-plane l_S scan on the reconstruction peak ($h_S = 0, k_S = 2.2$). The inset shows the peak width analysis.

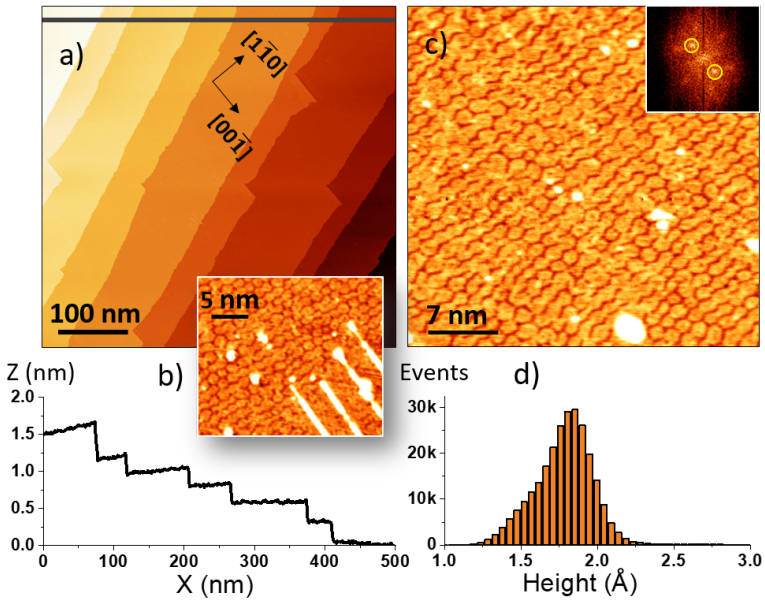

Figure 4: STM images ($U_b = 2.5$ V, $I_t = 0.05$ nA) of $Fe_{0.85}Al_{0.15}(110)$ surface annealed at 1193 K: a) Large scale image (500×500 nm^2) with a zoom (25×25 nm^2) showing carbon stripes. b) Profile along the line shown in Fig. a. c) High resolution (35×35 nm^2) image with Fourier analysis in inset; yellow circles highlight Fourier spots corresponding to the 15 Å periodicity. d) Apparent height histogram of Fig. a.

of $Fe_{1-x}Al_x$ alloys $\sim$ 2 eV above the Fermi level is mainly derived from Fe. Therefore, the dark borders of the "hexagons" and their inner part (Fig. 5) are probably more Al-rich.

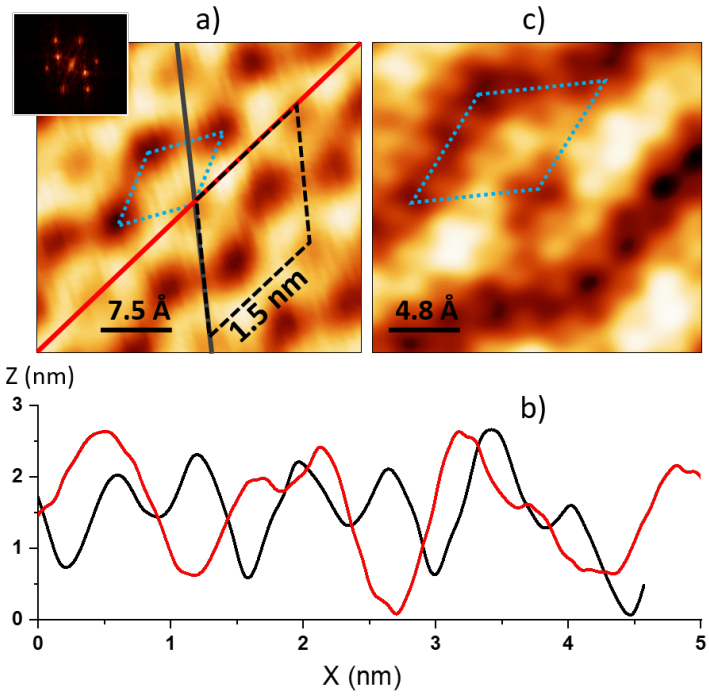

Figure 5: High resolution STM images (U_b = 2.5 V, I_t = 0.05 nA) of $Fe_{0.85}Al_{0.15}(110)$ surface annealed at 1193 K a) (3.75 × 3.75) nm^2 and b) (2.4 × 2.4) nm^2. Black and red lines in Fig. a are indicating profiles given in Fig. b. Black and blue rhombs highlight two periodic structures corresponding to reconstruction unit cell and areas with a lower density of states, respectively.

STM imaging matches also with GIXS findings. GIXS peak width analysis around integer positions both in radial and angular scans (not shown) points at a nearly constant reciprocal broadening of $\Delta q_A \simeq 0.05 - 0.06$ Å^{-1} for $(h_S \pm 0.44, k_S)$ and $\Delta q_B \simeq 0.03 - 0.04$ Å^{-1} for $(h_S \pm 0.22, k_S \pm 0.2)$. The corresponding coherence length of $1/\Delta q_A \simeq 16 - 20$ Å and $1/\Delta q_B \simeq 24 - 33$ Å is of the order of the modulation of the "hexagon". Besides those peaks that are similar to those found in LEED, broad bumps of FWHM $\Delta k_S \simeq 0.3$ are visible at $(0, k_s = 2.76, 4.76, 6.76)$ (Fig. 3-b) and also along the more complex

(h_S, h_S) direction (not shown). Those are reminiscent of a complex modulation of the unit cell content (position and/or composition) over a length $a_S/\Delta k_S \simeq 14$ Å.

3.2. The $Fe_{0.85}Al_{0.15}(100) - (1 \times 1)$ Al-rich surface

Starting from an annealing temperature of 673 K up to 1123 K, the LEED pattern of the (100) orientation is sharp and (1×1) (see Fig. 6-a) without any traces of reconstruction. Spots sharpen with temperature and $(n \times n)$ reconstructions can be ruled out from the Bragg angle estimated from screen-sample distance and screen size.

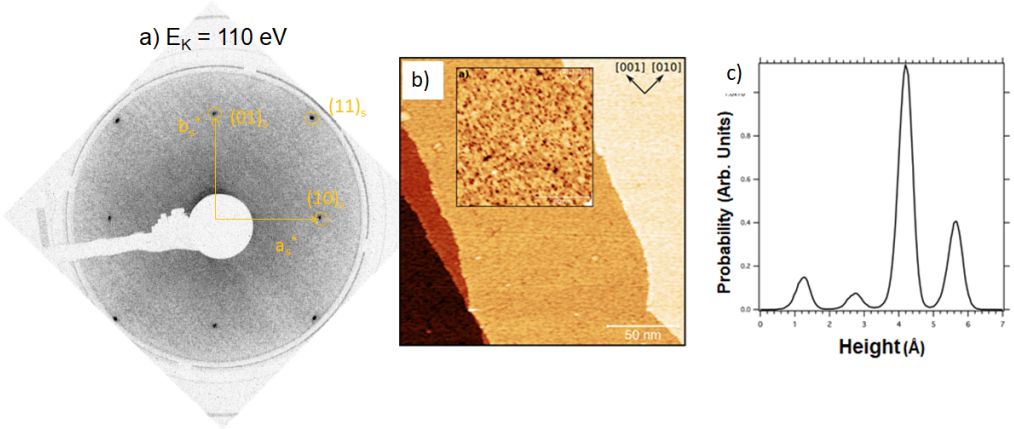

Figure 6: Structure of the $Fe_{0.85}Al_{0.15}(100)$ surface: (a)(1×1) LEED patterns after annealing at 973 K. Spot indexes are shown; (b) STM image after annealing at 1078 K (200×200 nm^2, $U_b = 0.9$ V, $I_t = 0.1$ nA) with a zoom in insert (50×50 nm^2, $U_b = 1.6$ V, $I_t = 0.4$ nA); (c) Corresponding histogram of the height of each pixel over the entire STM image.

Upon annealing at increasing temperatures, large scale STM images show that the $Fe_{0.85}Al_{0.15}(100)$ surface smoothens (Fig. S5 of Supplementary Material). Step edges tend to align along the compact $[10]_S = [001]_B$ direction with, however, a rather high density of kinks (Fig. 6-b). The step height agrees perfectly with the distance between atomic planes on the (100) surface [17] as shown by the histogram of Fig. 6-c where four terraces are clearly observed with a separation of 1.45 ± 0.07 Å. At higher magnification, the terraces appear flat at the atomic scale. The roughness calculated on each image

from $R_a = \frac{1}{N}\sum_{j=1}^{N} \mid z_j - \bar{z} \mid$ where z_j is the pixel height and $\bar{z}$ the average pixel height amounts to 0.34 ± 0.05 Å and 0.12 ± 0.02 Å, respectively, a value in agreement with typical metal corrugation.

The lack of reconstruction of the (1×1) structure during the progressive annealing of the $Fe_{0.85}Al_{0.15}(100)$ surface is in apparent discrepancy with the faint $c(2 \times 2)$ LEED structure observed by other groups at 648 K [22], 700 K [14] and slightly above 700 K [27]. According to XPS, competitive segregation of contaminants can be ruled out. The $c(2 \times 2)$ structure was previously assigned to an ordered top layer involving equal fractions of Al and Fe, although vacancies could not be excluded [14]. However, much sharper $c(2 \times 2)$ LEED patterns were obtained on crystals of rather similar composition, namely $Fe_{0.97}Al_{0.03}(100)$ and $Fe_{0.70}Al_{0.30}(100)$ [23, 14, 27, 22]. Such a sensitivity of the surface structure to the alloy bulk composition stems from the fact that $c(2\times2)$ reconstructions only appear for given surface Al/Fe relative concentrations [23, 27]. Indeed, on the $Fe_{0.85}Al_{0.15}(100)$ surface, the right Fe/Al ratio can be only achieved within a narrow temperature range [23, 27], which can explain that the $c(2 \times 2)$ was not observed herein. Conversely, the sharp (1×1) structure found on the Al-rich thick adlayer obtained by annealing above 1200 K (Fig. 6-a) is also systematically reported by other groups after annealing $Fe_{0.85}Al_{0.15}(100)$ surfaces well above 700 K [23, 14, 27, 22].

3.3. The nanometer-sized triangular-shaped pits of the $Fe_{0.85}Al_{0.15}(111)$ surface

For annealing temperature of 773 K up to 1273 K, the $Fe_{0.85}Al_{0.15}(111)$ orientation exhibits a (1×1) LEED pattern as shown in Fig. 7-a,b. No superstructure peak has ever been found. The evolution of the peak intensity with beam energy with an apparent 3-fold symmetry is due to the open structure of the (111) surface of bcc metals and to the reminiscence of the bulk extinctions. The surface unit cell $(\mathbf{a}_S, \mathbf{b}_S, \mathbf{c}_S)$ $(a_s = b_s = a_B\sqrt{2}, c_s = a_B\sqrt{3}/2)$ is occupied by three atoms at coordinates $(0,0,0)$, $(1/3, 2/3, 1/3)$ and $(2/3, 1/3, 2/3)$ leading to a structure factor with bulk extinctions when $h_S + 2k_S + l_S = 3n + 1$ and $h_S + 2k_S + l_S = 3n + 2$ with n integer (or $h_S + 2k_S + l_S = 3n + 2$ and $h_S + 2k_S + l_S = 3n + 1$). Therefore, for bulk diffraction, one over three Bragg peaks is active along the $(10l_S)$ and $(11l_S)$ rod but with an offset of $\Delta l_S = 1$ between the two types of rods. Since atoms of the (111) surface are not coplanar and the surface is nanofaceted (see below), this conclusion partially applies to LEED despite the poor penetration

depth of electrons and the weakness of kinematic interpretation in LEED.

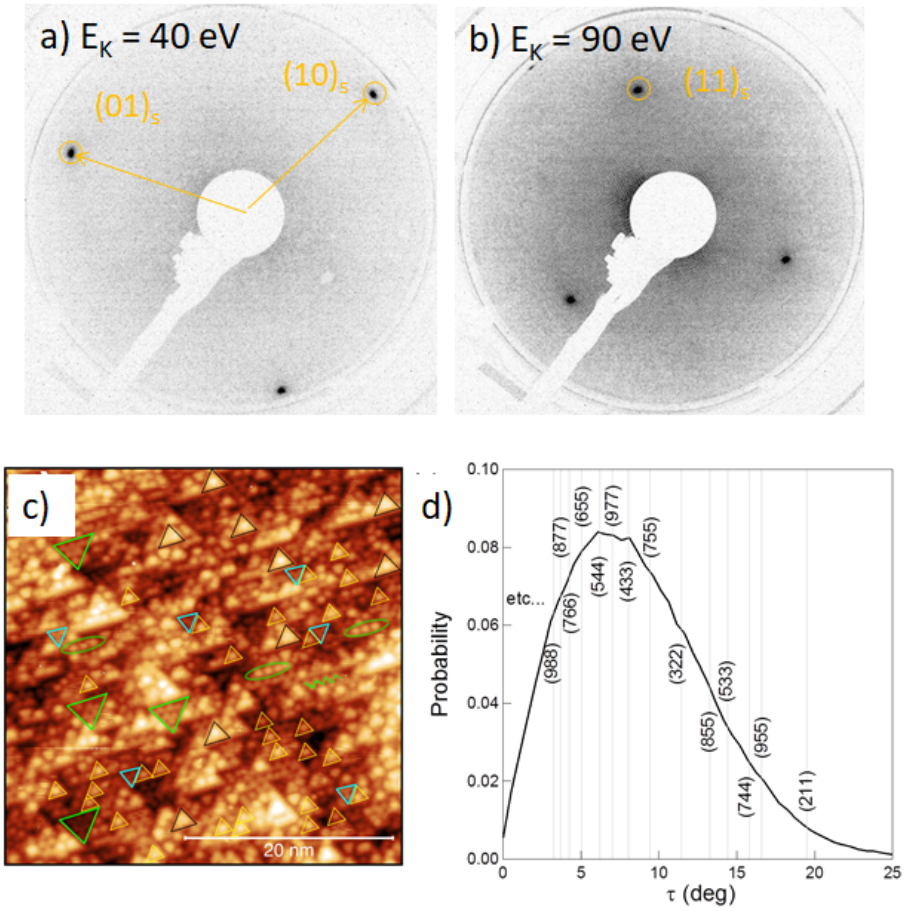

Figure 7: $Fe_{0.85}Al_{0.15}(111)$ after annealing at 973 K: Evolution with beam energy of the LEED pattern at a) 40 eV and b) 90 eV. c) STM image (38×38 nm^2, $U_b = -1.5$ V, $I_t = 0.4$ nA) with highlighted features: pyramidal protrusions (black and yellow triangles), holes with an internal periodicity (blue and green triangles) and chains (green ellipses). d) Local slope distribution τ of image c. The values for (111) vicinal surfaces of type (hkk) with $h \leq 9$ and $k < h$ are marked.

The smoothing of the (111) surface with increasing temperature is even more apparent than on the other two orientations. On large scale images (500×500 nm^2, Fig. S5 of Supplementary Material), sputtering induces long range undulations with amplitudes of several nanometers and corre-

lation lengths of several hundreds of nanometers. Upon annealing between 785 K and 1186 K, the roughness parameter R_a drops by an order of magnitude (from 1 nm to 0.1 nm). However, at higher magnification (Fig. 7-c), nanometer-sized triangular-shaped pits appear that are aligned along the $[10]_S = [1\bar{1}0]_B$ and the three-fold equivalent directions. They have a size of around 1-2 nm and are organized as shown in Fig. 7-c. This topographic appearance can be understood by the open character of (111) surface of bcc metals which exhibits three different non-coplanar levels distant by $a_B/2\sqrt{3} = 0.83$ Å. Height distribution histograms correspond to different atomic planes separated by 0.72 Åas shown in Fig. S6 of Supplementary Material. The local slopes τ of the largest protrusions found in Fig. 7-c feature nanopyramids with (111) vicinal side facets.Bcc (111) vicinal planes are derived from an alternance of small (211) facets and steps (Fig. S7 of Supplementary Material). Line cuts along three equivalent $[21]_S = [1\bar{2}1]_B$ directions and normal to the $[10\bar{1}]_B$ pyramid edges (Fig. S8 of Supplementary Material) give a local slope of 8.5° very close to the $\tau = 8.05°$ of the (433) vicinal orientation. In a global analysis of τ on image Fig. 7-c, the three-fold symmetric distribution is dominated by τ values around $6 - 7°$ with a very poor contribution from flat areas. The expected angles for vicinal (hkk) surfaces $(h > k)$ relative to (111) are given by $\cos\tau = \frac{h+2k}{\sqrt{3}\sqrt{h^2+2k^2}}$. They are shown as grey lines in Fig. 7-d. The slope density peaks around (655), (544), (977) and (433) orientations. The three equivalent $(hkk), (khk), (kkh)$ form nanopyramids with downhill edges along the $[11\bar{3}]_B, [1\bar{3}1]_B$ and $[\bar{3}11]_B$ directions. The symmetric orientations corresponding to pyramids rotated by 180° do not appear, likely because of a miscut of the sample.

The present findings are in line with previous observations of servere multilayer segregation on the open (111), (211) and (310) FeAl surfaces but with the lack of any previously observed reconstructions [20]. Aluminum segregation may favor nanofacetting as it is known for other atomically rough and non-close-packed surfaces of high surface free energy when covered with a foreign element [43, 44]. For instance, with adsorbed oxygen or deposited metals, bcc W(111)/Mo(111), fcc Ir(210)/Pt(210) and hc (hexagonal compact) Re($12\bar{3}1$) spontaneously rearrange above 700 K to minimise their total surface energy by developping facets even if it involves an increase in surface area and step/kink energy. Faceting on W(111) develops (211) facets upon O, Pt, Pd adsorption [45, 44, 43]. On such bcc (111) surfaces, one physical

monolayer of foreign element is required; it corresponds to three atomic (111) planes; more material leads to islanding or alloying. Most of the time the facets formed are more close-packed than the initial ones and facetting keeps the symmetry of the initial surface (C_{3v} in the case of $Fe_{0.85}Al_{0.15}(111)$). The facetting driving force is thermodynamic, namely a reduced surface energy of the covered vicinal surface compared to the flat surface. According to calculations [46], this is already verified in the case of bare iron; the extended (211) surface has a lower energy than the open (111) surface ($E_{Fe}^{(111)} = 2.73$ J.m^{-2}; $E_{Fe}^{(211)} = 2.59$ J.m^{-2}). But faceting is also controlled by step and kink energies, entropy, kinetics and mass transport. In our case, nano-facetting is observed upon aluminum segregation like in the case of sulfur on Fe(111) [47] and seems homogeneous since nanopyramids do not coexist with the planar surface (Fig. 7-b). Usually, faceting by an adsorbate is limited to a given temperature window before the onset of desorption of the foreign element; above that temperature the surface flattens again. However in the present case, segregation of aluminum provides an infinite reservoir; despite the increase of temperature, the $Fe_{0.85}Al_{0.15}(111)$ surface smoothens but never flattens. Finally, at the opposite of metal covered W(111), not only (211) facets are observed on $Fe_{0.85}Al_{0.15}(111)$) but also (111) vicinals maybe because of the complex interplay between segregation, surface alloy formation and faceting.

At last, few areas appear locally flat at the atomic scale with an hexagonal periodicity (green triangle in the bottom-left corner of Fig. 7 and Fig. S9 of Supplementary Material along bulk directions of ~ 8 Å which is the double of the surface lattice parameter ($a_S = 4.01$ Å). A likely hypothesis is local ordering of the segregated aluminum atoms in a B_2-CsCl structure in agreement with the $Fe_{0.5}Al_{0.5}$ surface composition found in XPS. Indeed on the FeAl(111), the surface lattice spacing is 7.35 Å.

4. Conclusion

As seen by photoemission [17], annealing induces an enrichment of the subsurface of the $Fe_{0.85}Al_{0.15}$ bcc random alloy over a typical length scale of 2.5-3 nm with a surface composition close to $Fe_{0.5}Al_{0.5}$ for the (100) and (111) orientations and close to $Fe_{0.6}Al_{0.4}$ for the (110). The orientation dependence of the surface structures was scrutinized by LEED, STM and GIXD. The segregation of aluminum is accompanied by (i) the appearance of a non-commensurate complex long-range structural/chemical superstructure with

a pseudo-hexagonal unit cell of $\sim$ 18 Å on the (110) surface extending approximately over 4 atomic planes, (ii) a (1×1) termination on the (100) surface and (iii) an intense faceting in the form of triangular pits having vicinal (111) side facets for the (111) orientation. The faceting of the (111) surface is assigned to the open character of the bcc (111) orientation and to the lower surface energy of (211) facets from which are derived the (111) vicinal planes. Further work is required to elucidate the complex (110) Al-rich superstructure.

5. acknowledgments

The PhD thesis of Z.D. was funded by the Chinese Scholarship Council. The present work benefited from the support of "Agence Nationale de la Recherche" - France in the frame of project SURFOX, (ANR-16-CE08-0034-01). Synchrotron diffraction experiments were supported by the French state funds Equipex ANR-11-EQPX-0010.

References

[1] A. Mertens, E. M. Bellhouse, J. R. McDermid, Microstructure and mechanical properties of a mixed SiAl TRIP-assisted steel subjected to continuous galvanizing heat treatments, Materials Science and Engineering: A 608 (2014) 249 – 257 (2014).

[2] S.-H. Kim, H. Kim, N. J. Kim, Brittle intermetallic compound makes ultrastrong low-density steel with large ductility, Nature 518 (2015) 77 (2015).

[3] S. Deevi, V. Sikka, Nickel and iron aluminides: An overview on properties, processing, and applications, Intermetallics 4 (5) (1996) 357–375 (1996).

[4] D. G. Morris, M. A. Muñoz Morris, J. Chao, Development of high strength, high ductility and high creep resistant iron aluminide, Intermetallics 12 (7) (2004) 821 – 826 (2004).

[5] M. Palm, Concepts derived from phase diagram studies for the strengthening of FeAl-based alloys, Intermetallics 13 (12) (2005) 1286 – 1295 (2005).

[6] A. R. Marder, The metallurgy of zinc-coated steel, Prog. Mater Sci. 45 (3) (2000) 191 – 271 (2000).

[7] P. Drillet, Z. Zermout, D. Bouleau, J. Mataigne, S. Claessens, Selective oxidation of high Si, Mn and Al steel grades during recrystallization annealing and steel/Zn reactivity, La Revue de Métallurgie-CIT 101 (10) (2004) 831–837 (2004).

[8] R. Cavallotti, J. Goniakowski, R. Lazzari, J. Jupille, A. Koltsov, D. Loison, Role of surface hydroxyl groups on zinc adsorption characteristics on $\alpha-Al_2O_3(0001)$ surfaces: first-principles study, J. Phys. Chem. C 118 (2014) 13578–13589 (2014).

[9] R. Cavallotti, Effets de la terminaison de l'α-alumine sur le comportement au mouillage du zinc, Ph.D. thesis, Pierre and Marie Curie University, France (2014).

[10] R. Cavallotti, H.-L. Thi Le, J. Goniakowski, R. Lazzari, J. Jupille, A. Koltsov, D. Loison, New routes for engineering the adhesion at $Zn/\alpha-Al_2O_3(0001)$ interface, Phys. Chem. Chem. Phys. 18 (2016) 3032–3039 (2016).

[11] H.-A. T. Le, J. Goniakowski, C. Noguera, A. Koltsov, J.-M. Mataigne, First-principles study on the effect of pure and oxidized transition-metal buffers on adhesion at the alumina/zinc interface, J. Phys. Chem. C 120 (2016) 9836–9844 (2016).

[12] H.-L. Thi Le, R. Lazzari, J. Goniakowski, S. Cavallotti, R. Chenot, C. Noguera, J. Jupille, A. Koltsov, J.-M. Mataigne, Tuning adhesion at metal/oxide interfaces by surface hydroxylation, J. Phys. Chem. C 121 (2017) 11464–11471 (2017).

[13] Z. Liu, Y. Chang, Thermodynamic assessment of the Al-Fe-Si system, Metall. Mater. Trans. A 30 (4) (1999) 1081–1095 (1999).

[14] V. Blum, L. Hammer, W. Meier, K. Heinz, M. Schmid, E. Lundgren, P. Varga, Segregation and ordering at $Fe_{1-x}Al_x$ (100) surfaces : a model case for binary alloys, Surf. Sci. 474 (1) (2001) 81–97 (2001).

[15] B. Predel, Al-Fe (Aluminum-Iron), in: Ac-Ag ... Au-Zr: Supplement to Subvolume IV/5A, Landolt-Börnstein-Group IV Physical Chemistry

12A: Physical Chemistry, Springer-Verlag Berlin Heidelberg, 2006, pp. 1–2 (2006).

[16] O. Kubaschewski, Iron binary phase diagrams, Springer Science & Business Media, 2013 (2013).

[17] Z. Dai, P. Borghetti, S. Chenot, P. David, J. Jupille, G. Cabailh, J. Goniakowski, R. Lazzari, Aluminium segregation profiles in the (110), (100) and (111) surface regions of the $Fe_{0.85}Al_{0.15}$ random body-centered cubic alloy, Appl. Surf. Sci. 492 (2019) 886–895 (2019).

[18] Z. Dai, Orientation-dependent segregation and oxidation at $Fe_{0.85}Al_{0.15}$ random alloy surfaces, Ph.D. thesis, University Pierre et Marie Curie, France (2017).

[19] M. Kottcke, H. Graupner, D. Zehner, L. Hammer, K. Heinz, Segregation-induced subsurface restructuring of FeAl (100), Phys. Rev. B 54 (8) (1996) R5275 (1996).

[20] L. Hammer, H. Graupner, V. Blum, K. Heinz, G. Ownby, D. Zehner, Segregation phenomena on surfaces of the ordered bimetallic alloy FeAl, Surf. Sci. 412-413 (1998) 69–81 (1998).

[21] M. Gemmaz, M. Afyouni, A. Mosser, Determination of the diffusion coefficient of Al in Fe-Al alloy by Auger spectrometry, Surf. Sci. Lett. 227 (1990) L109–L11 (1990).

[22] B. Eltester, C. Uebing, H. Viefhaus, H. Grabke, AES and LEED investigation of Al segregation and oxidation of the (100) face of $Fe_{85}Al_{15}$ single crystals, Fresen. J. Anal. Chem. 358 (1-2) (1997) 196–199 (1997).

[23] W. Meier, V. Blum, L. Hammer, K. Heinz, Equilibration of stoichiometrically distorted $Fe_{1-x}Al_x$ (100) surfaces, J. Phys.: Condens. Matter 13 (9) (2001) 1781–1791 (2001).

[24] H. Graupner, L. Hammer, K. Müller, D. Zehner, Composition and structure of the (100) and (110) surfaces of FeAl, Surf. Sci. 322 (1995) 103–115 (1995).

[25] K. Heinz, L. Hammer, Surface structure and segregation of bimetallic bcc-type alloys, J. Phys.: Condens. Matter 11 (43) (1999) 8377 (1999).

[26] V. Blum, L. Hammer, W. Meier, K. Heinz, Quantification of substitutional disorder and atomic vibrations by LEED-the role of parameter correlations, Surf. Sci. 488 (1) (2001) 219–232 (2001).

[27] L. Hammer, W. Meier, V. Blum, K. Heinz, Equilibration processes in surfaces of the binary alloy Fe-Al, J. Phys: Condens. Matter 14 (2002) 4145–4164 (2002).

[28] Z. Dai, P. Borghetti, Y. Mouchaal, S. Chenot, P. David, J. Jupille, G. Cabailh, R. Lazzari, Self-organized carbon-rich stripe formation from competitive carbon and aluminium segregation at $Fe_{0.85}Al_{0.15}$(110) surfaces, Appl. Surf. Sci. 444 (2018) 457–466 (2018).

[29] I. Horcas, R. Fernández, J. M. Gómez-Rodríguez, J. Colchero, J. Gómez-Herrero, A. M. Baro, Wsxm: A software for scanning probe microscopy and a tool for nanotechnology, Review of Scientific Instruments 78 (1) (2007) 013705 (2007).

[30] Gwyddion software, http://gwyddion.net/.

[31] D. Necas, P. Klapetek, Gwyddion: an open-source software for SPM data analysis, Cent. Eur. J. Phys. 10 (2012) 181–188 (2012).

[32] http://www.physik.de/mateck.

[33] R. Baudoing-Savois, M. De Santis, M. Saint-Lager, P. Dolle, O. Geaymond, P. Taunier, P. Jeantet, J. Roux, G. Renaud, A. Barbier, A new UHV diffractometer for surface structure and real time molecular beam deposition studies with synchrotron radiations at ESRF, Nucl. Inst. Meth. Phys. Res. B 149 (1999) 213–227 (1999).

[34] G. Renaud, R. Lazzari, F. Leroy, Probing surface and interface morphology with grazing incidence small angle X-ray scattering, Surf. Sci. Rep. 64 (2009) 255–380 (2009).

[35] L. B. N. Laboratory, Center for X-ray optics, http://www-cxro.lbl.gov/.

[36] M. Ellner, I. Park, On the partial atomic volume of aluminum in solid solutions based on the 3d transition metals and copper, Metallurgical and Materials Transactions A 33 (2002) 3591–3595 (2002).

[37] LEEDpat, Version 4.2, utility by K.E. Hermann (FHI) and M.A. Van Hove (HKBU), Berlin / Hong Kong, 2014; see also http://www.fhi-berlin.mpg.de/KHsoftware/LEEDpat/index.html.

[38] O. Kizilkaya, D. Hite, D. Zehner, P. Sprunger, Surface reconstruction of FeAl(110) studied by scanning tunnelling microscopy and angle-resolved photoemission spectroscopy, J. Phys.: Condens. Matter 16 (30) (2004) 5395–5406 (Jul 2004).

[39] A. Baddorf, S. Chandavarkar, Identification of an incommensurate $FeAl_2$ overlayer on FeAI(110) using x-ray diffraction and reflectivity, Physica B 221 (1996) 141–144 (1996).

[40] O. Kizilkaya, I. Senevirathne, P. Sprunger, The electronic structure of ultrathin aluminum oxide film grown on FeAl (110): A photoemission spectroscopy, J. Appl. Phys. 101 (6) (2007) 063706 (2007).

[41] G. Das, B. Rao, P. Jena, S. Deevi, Electronic structure of substoichiometric Fe-Al intermetallics, Phys. Rev. B 66 (18) (2002) 184203 (2002).

[42] T. Duguet, P. A. Thiel, Chemical contrast in STM imaging of transition metal aluminides, Prog. Surf. Sci. 87 (2012) 47 – 62 (2012).

[43] T. E. Madey, W. Chen, P. Wang, Kaghazchi, T. Jacob, Nanoscale surface chemistry over faceted substrates: structure, reactivity and nanotemplate, Chem. Soc. Rev. 37 (2008) 2310–2327 (2008).

[44] C. Revenant, F. Leroy, G. Renaud, R. Lazzari, A. Letoublon, T. Madey, Structural and morphological evolution of Co on faceted Pt/W(111) surface upon thermal annealing, Surf. Sci. 601 (2007) 3431–3449 (2007).

[45] A. Szczepkowicz, A. Ciszewski, R. Bryl, C. Oleksy, C.-H. Nien, Q. Wu, T. E. Madey, A comparison of adsorbate-induced faceting on flat and curved crystal surfaces, Surface Science 599 (1) (2005) 55 – 68 (2005).

[46] L. Vitos, A. Ruban, H. Skriver, J. Kollár, The surface energy of metals, Surf. Sci. 411 (1998) 186 (1998).

[47] S. Lin, H. Cabibil, J. A. Kelber, S-induced faceting transformations on fe(111), Surf. Sci. 395 (1) (1998) 30 – 42 (1998).